Tomographic reconstruction for wide-field adaptive optics systems: Fourier domain analysis and fundamental limitations

Benoit Neichel,[1,2,*] Thierry Fusco,[1,2] and Jean-Marc Conan[1,2]

[1]*ONERA, BP72, 92322 Chatillon Cedex, France*
[2]*Groupement d'Intérêt Scientifique PHASE (Partenariat Haute résolution Angulaire Sol Espace) between ONERA, Observatoire de Paris, CNRS, and University Denis Diderot, Paris 7*
*Corresponding author: benoit.neichel@onera.fr

Several wide-field-of-view adaptive optics (WFAO) concepts such as multi-conjugate AO (MCAO), multi-object AO (MOAO), and ground-layer AO (GLAO) are currently being studied for the next generation of Extremely Large Telescopes (ELTs). All these concepts will use atmospheric tomography to reconstruct the turbulent-phase volume. In this paper, we explore different reconstruction algorithms and their fundamental limitations, conducting this analysis in the Fourier domain. This approach allows us to derive simple analytical formulations for the different configurations and brings a comprehensive view of WFAO limitations. We then investigate model and statistical errors and their effect on the phase reconstruction. Finally, we show some examples of different WFAO systems and their expected performance on a 42 m telescope case. © 2008 Optical Society of America

OCIS codes: 010.1080, 010.1330.

1. INTRODUCTION

For the next generation of Extremely Large Telescopes (ELTs), several wide-field adaptive optics (WFAO) concepts such as ground-layer AO (GLAO), multi-conjugate AO (MCAO), laser tomography AO (LTAO), and multi-object AO (MOAO) have been proposed. These systems will play a crucial role, since most of them could be used as first-light instruments. It is then of prime importance to understand the fundamental limitations, the possible optimizations, and the expected performance of these systems. The goal of this paper is to bring a qualitative and quantitative analysis of the most general problem of phase reconstruction and correction in multi-guide star (GS) AO. We try to point out some general trends shared by all these future systems, and we propose physical interpretations of the results.

All these WFAO concepts have in common that they require knowledge of three-dimensional turbulence volume. The method for measuring three-dimensional atmospheric phase perturbations was proposed by Tallon and Foy [1]: light from several GSs is used to probe the instantaneous three-dimensional phase perturbations, and the turbulence volume is then reconstructed by solving an inverse problem. This technique, called atmospheric tomography, was later improved by Johnston and Welsh [2], Ellerbroek [3], and Fusco *et al.*, among others [4]. The tomographic reconstruction error depends only on the GSs' constellation, atmospheric conditions, and wave front Sensor (WFS) characteristics. The geometry of the system sets the first two fundamental limitations of the tomography: unseen modes and unseen turbulence. Unseen turbulence that originates from partial pupil overlap can

play a nonnegligible role in the global residual variance (e.g., [5,6]); however, in the framework of ELTs this term becomes negligible [7]. We therefore choose to neglect the error due to unseen turbulence in the present study. Instead, in the first part of this paper, we focus on unseen modes and their effect on the phase estimation depending on the reconstructor choice.

In addition to this fundamental limitation, in the second part of this paper, we investigate an additional term due to model/statistical errors. This term comes from a faulty knowledge of system and atmospheric conditions, which limits the tomographic reconstruction. For instance, Conan *et al.* [8] and Tokovinin and Viard [9] have studied the sensitivity of the reconstruction error to an error on the Cn2 profile; LeLouarn and Tallon [10] have explored the influence of the reconstructed turbulent layers' altitudes compared with the real turbulence volume; and Fusco *et al.* [11] have studied the effect of a reconstruction on a limited number of equivalent layers (ELs). All these studies suggest that the tomography is particularly robust to model/statistical errors. We generalize these approaches for the ELTs and try to provide a comprehensive study of the effect of these model errors.

Once the three-dimensional turbulence volume is reconstructed, different types of corrections can be applied. The correction step consists of a projection of the reconstructed tomographic phase on the deformable mirrors (DMs). It depends only on the number and position of the DMs with respect to the reconstructed layers, and the optimization area. If the corrected area is not increased compared with the case in classical AO, only one DM conjugated to the telescope pupil is required to perform the

correction (MOAO, LTAO). The main advantage of those methods is that any target selected in the field of view (FoV) can be corrected: thus the sky coverage is significantly increased. Moreover, there are no additional terms of errors due to projection. For a larger corrected field, a trade-off between the optimization area and the DMs' position is applied. This additional error term was defined by Rigaut *et al.* [12] and Tokovinin *et al.* [13] as generalized fitting. For instance, with one DM conjugated to the telescope pupil (GLAO), a wide field can be corrected uniformly; however, the performance is dramatically limited by this error term. To reduce the effect of the generalized fitting, one must use more DMs that are optically conjugated to the turbulence volume. By correcting the turbulece volume above the telescope, the efficiency of the correction is significantly improved (MCAO). In the third part of the paper, we investigate this particular error term and its implications for ELTs. We compare the relative performance expected for the different WFAO concepts, explore the effect of different reconstructors, and discuss the choice of the number of DMs.

We choose to conduct all these analyses in the Fourier spatial frequency domain because it allows us to perform a fast investigation of the parameter space, and it brings a comprehensive view of the effect of the different terms. The use of spatial-frequency-domain techniques was initially proposed by Rigaut *et al.* [14], who derived the analytical expressions for the five most fundamental limits of any natural guide star (NGS)-based AO system: fitting error, angular anisoplanatism, servo-lag, WFS noise, and WFS aliasing. This single conjugated NGS-AO case was later extended by Jolissaint *et al.* [15], who included the correlation between anisoplanatism and servo-lag error and generalized the formalism for two-dimensional systems. On the other hand, Tokovinin and colleagues [9,13] have proposed an approach for evaluating the wavefront fitting error with a limited number of DMs in a MCAO system (the so-called generalized fitting) and the tomographic reconstruction error from a limited number of noisy measurements (see also [16]). Following their approach, Gavel [17] has generalized the optimal tomographic reconstruction for spherical waves. Although this approach requires some simplifications, it allows treatment of the so-called "focus anisoplanatism" error. Finally, Ellerbroek [18,19] has derived an integrated approach that takes into account the fundamental error sources and their correlations for the general case of multi-GS AO and MCAO.

We follow Ellerbroek's approach, with additional developments to account for model errors and a different formalism. For sake of simplicity, we choose not to include temporal behaviors, aliasing effects, or closed-loop considerations. In addition, we will consider only NGSs. This NGS open-loop hypothesis could appear to be restrictive; however, it allows us to obtain simple analytical formulas. Considering the complexity of WFAO systems, it is instructive to isolate specific factors in order to disentangle their individual effects. All these terms can later be included, for instance, in a second step or for a real system design.

In Section 2 we briefly summarize the theoretical basis of Fourier simulation, and in Section 3 we apply this method to WFAO. In Section 4 we describe the simulation cases used thoroughout the paper. Section 5 is devoted to pure tomographic reconstruction and the effect of unseen frequencies. In Section 6 we investigate the effect of model errors on the tomographic phase reconstruction and in Section 7 the effect of statistical errors. Finally, Section 8 focuses on phase control and projection on DMs with some examples of different WFAO systems and their expected performance for a 42 m telescope. Conclusions are given in Section 9.

2. FOURIER AO MODELING

A. Introduction to Fourier Simulations
The starting point of the Fourier method is to assume that the optical system (phase propagation, WFS measurements, DMs commands) is linear and spatially shift invariant. In that case, all the usual operators are diagonals with respect to the spatial frequencies and simply act as spatial filters in the Fourier domain. Therefore, each equation can be written frequency by frequency. For instance, the tomographic phase reconstruction is derived and evaluated one Fourier component at a time. In addition, our purpose is to derive regularized reconstructors that make use of the knowledge of the phase and noise statistics. Therefore, these statistics must also be described by linear shift-invariant spatial filters. This is achieved by assuming Gaussian and stationary statistics. In that case, the phase and noise statistics can be entirely characterized by their second-order moments—more precisely, by their power spectral density (PSD). As a consequence, the residual phase in the pupil for one direction of interest is itself fully characterized by its PSD. We will make use of this residual phase PSD to carry our analysis. This is similar to the usual characterization of the turbulent phase by the Kolmogorov/Von Karman PSD except that we derive a PSD for the residual phase. Similarly to what is usually done for the turbulent phase, we can then from this residual phase PSD (i) construct the phase structure function, the optical transfer function, and the long exposure PSF, (ii) compute the residual phase variance, and (iii) generate instantaneous corrected phase screens and instantaneous AO corrected PSFs. The derivation of the residual phase PSD for the WFAO system is described in Section 3.

The main advantage of the Fourier method is that the computational complexity is significantly reduced compared with that in spatial domain modeling. The main limitation is that aperture-edge effects and boundary conditions, which cannot be represented by shift-invariant spatial filters, are neglected. Therefore, the Fourier modeling applies only to the ideal case of infinite-aperture systems. Note that this applies only to the calculation of the PSD, since for performance evaluation we will be able to account for a finite aperture (see, e.g., Subsection 2.B). The main assumption is then that all the effects of incomplete beam overlap in the upper atmospheric layers are neglected. The effect of such an assumption is discussed in [7], based on a comparison with a full E2E simulation code. Briefly, it is shown that as long as the different beams are superimposed in the upper layer, the error due to unseen turbulence has no effect on the tomographic re-

construction. For a 42 m telescope and a typical atmospheric profile, this would correspond to a maximum GS diameter constellation of around 8 arcmin.

B. From PSD to Variance and Strehl Ratio

In the following, we will characterize performance in term of residual variance and Strehl ratio (SR). Following Ellerbroek [19] and Jolissaint [15], we define the residual phase variance as the piston-filtered integral of the residual phase PSD. This reads

$$\sigma^2_{res,\theta} = \int_0^\infty \mathrm{PSD}^{res}_\theta(f)F_p(f)\mathrm{d}f \tag{1}$$

with

$$F_p(\mathbf{f}) = 1 - \left[\frac{2J_1(\pi Df)}{\pi Df} \right]^2, \tag{2}$$

where D is the telescope pupil diameter. Throughout this paper, D is set to 42 m. The SR is derived from the long-exposure PSF, which is computed from the PSD as described by Jolissaint *et al.* [15]

3. FOURIER WFAO MODELING

The goal of this section is to derive the residual PSD when dealing with WFAO systems.

A. System Description and Notation

The atmospheric profile will be divided into N_L discrete independent layers located at altitudes $\{h_n\}$. Each turbulent layer is described by its own power spectrum C_{φ_n}, which can be written for the nth layer as

$$C_{\varphi_n} = \lambda_n C_\phi, \tag{3}$$

where C_ϕ is a Von Kármán power spectrum defined by

$$C_\phi(\mathbf{f}) = 0.023\left(\frac{1}{r_0}\right)^{5/3}\left(\mathbf{f}^2 + \frac{1}{L_0}\right)^{-11/6}, \tag{4}$$

where r_0 is the Fried parameter and L_0 is the outer scale of turbulence. In the following, we implicitly assume that all the layers have the same value of L_0. λ_n is the fraction of turbulent energy located in the nth layer and is defined by

$$\lambda_n = C_n^2(h_n)\delta h_n \bigg/ \sum_{n=1}^{N_L} C_n^2(h_n)\delta h_n, \tag{5}$$

where δh_n represents the width of each turbulent layer. We can then write that $C_\phi = \Sigma_{n=1}^{N_L}\lambda_n C_\phi = \Sigma_{n=1}^{N_L}C_{\varphi_n}$. The measurement is performed with several WFSs, each WFS looking at one GS. The number of GSs/WFSs is denoted N_{gs}, and the associated GS positions are given by $\alpha = \{\alpha_i\}$.

The correction is performed by N_{DM} DMs, optically conjugated to altitudes $\{h_n^{DM}\}$. The FoV of interest, where the correction has to be optimized, is discretized into N_{ang} angles $\beta = \{\beta_j\}$. Finally, performance is computed for N_{dir} direction of interests, at angles $\theta = \{\theta_k\}$. Figure 1 summarizes the geometry of the system.
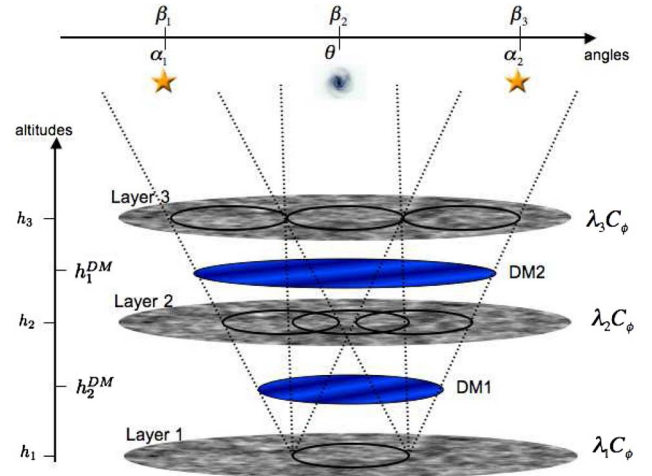

Fig. 1. (Color online) Illustration of the system geometry. In this example, the atmosphere is simulated with three layers at altitudes $h_{n=1,2,3}$, weighted by a $\lambda_{n=1,2,3}$ factor ($\Sigma_{n=1}^{N_L}\lambda_n = 1$). Two guide stars are considered in directions $\alpha_{i=1,2}$, the optimization is done in three directions $\beta_{j=1,2,3}$, the correction is perfomed with two DMs at altitudes $h_{n=1,2}^{DM}$, and the final performance is evaluated in one direction θ.

B. Residual Phase, Measurement Equation, and DM Command

We start with the calculation of the residual phase, expressed in the Fourier domain. In the direction of interest θ, the residual phase $\widetilde{\phi}^{res}_\theta(\mathbf{f})$ is given by the difference between the atmospheric phase corrugation $\widetilde{\phi}_\theta(\mathbf{f})$ and the correction phase $\widetilde{\phi}^{corr}_\theta(\mathbf{f})$:

$$\widetilde{\phi}^{res}_\theta(\mathbf{f}) = \widetilde{\phi}_\theta(\mathbf{f}) - \widetilde{\phi}^{corr}_\theta(\mathbf{f}), \tag{6}$$

where the tilde denotes the Fourier transform. Assuming that propagation effects can be neglected, the turbulent phase resulting in the pupil when looking in the direction θ can be expressed as the sum of all phase perturbations. With the Fourier shift property, it leads to

$$\widetilde{\phi}_\theta(\mathbf{f}) = \sum_{n=1}^{L} \widetilde{\varphi}_n(\mathbf{f})e^{2j\pi\mathbf{f}h_n\theta}, \tag{7}$$

where $\widetilde{\varphi}_n$ is the phase corresponding to the nth layer.

The correction phase is the sum of the phase perturbations introduced by the DMs. This resulting correction phase in the direction θ then reads

$$\widetilde{\phi}^{corr}_\theta(\mathbf{f}) = \sum_{n=1}^{N_{DM}} \widetilde{\varphi}_n^{DM}(\mathbf{f})e^{2j\pi\mathbf{f}h_n^{DM}\theta}, \tag{8}$$

where $\widetilde{\varphi}_n^{DM}$ is the correction phase done by the nth DM. Note that each DM is assumed to correct spatial frequencies up to a cut-off frequency f_c^{DM},

$$f_c^{DM} = N_{act}/2D, \tag{9}$$

where N_{act} is the actuator pitch as seen from the pupil plane. Beyond this cut-off frequency, no correction is applied and the corresponding phase $\widetilde{\varphi}_n^{DM}(|\mathbf{f}| > f_c^{DM}) = 0$.

To simplify the equations, in the following we adopt the notation $\tilde{x}$, which refers to $\tilde{x}(f)$ at a given frequency. For each frequency, Eqs. (7) and (8) can then be written in a vectorial form:

$$\tilde{\phi}_\theta = \mathbf{P}_\theta^{\mathbf{L}} \varphi_{\mathbf{turb}}, \qquad \tilde{\phi}_\theta^{corr} = \mathbf{P}_\theta^{\mathbf{DM}} \tilde{\varphi}_{\mathbf{DM}}, \qquad (10)$$

where $\tilde{\phi}_\theta$ and $\tilde{\phi}_\theta^{corr}$ are scalar. $\mathbf{P}_\theta^{\mathbf{L}}$ and $\mathbf{P}_\theta^{\mathbf{DM}}$ are line vectors of sizes N_L and N_{DM}, respectively, $\tilde{\varphi}_{\mathbf{turb}}$ is a column vector of size N_L that concatenates the N_L turbulent phases $\{\tilde{\varphi}_{\mathbf{n}}\}$. Similarly, $\tilde{\varphi}_{\mathbf{DM}}$ is a column vector of size N_{DM} gathering the N_{DM} correction phases $\{\tilde{\varphi}_n^{DM}\}$.

$\mathbf{P}_\theta^{\mathbf{L}}$ projects the N_L turbulent layers seen in the θ direction in the pupil plane, and $\mathbf{P}_\theta^{\mathbf{DM}}$ projects the DM phases seen in the θ direction in the pupil. The elements of the vectors $\mathbf{P}_\theta^{\mathbf{L}}$ and $\mathbf{P}_\theta^{\mathbf{DM}}$ are simply the complex exponential appearing, respectively, in Eq. (7) and Eq. (8).

In the following we will assume that each measurement from the WFS is divided in two submeasures, called hereafter measurement along x and y. For instance, this corresponds to x and y slopes when one is considering a Shack–Hartmann (SH) sensor. In that case, the most general form of the measurement is to write it as (for a given frequency)

$$\tilde{\phi}^{\mathbf{meas}} = \mathbf{M}\mathbf{P}_\alpha^{\mathbf{L}} \tilde{\varphi}_{\mathbf{turb}} + \mathbf{b}, \qquad (11)$$

where $\tilde{\phi}^{\mathbf{meas}}$ is a ($2N_{gs}$) column vector that concatenates the measurements coming from the N_{gs} GSs.

$\mathbf{P}_\alpha^{\mathbf{L}}$ is a matrix of size $N_L \times N_{gs}$, where we adopt the convention "columns by rows," which projects the phases in altitudes coming from the N_{gs} α_i directions in the pupil. Similarly to $\mathbf{P}_\theta^{\mathbf{L}}$, each line of the $\mathbf{P}_\alpha^{\mathbf{L}}$ matrix is filled with a phase-shift complex exponential, θ being replaced by the α_i direction of the considered GS.

$\mathbf{M}$ is a matrix that models the WF sensing operation (see, e.g., Rigaut *et al.* [14] and Jolissaint *et al.* [15], for an expression of the SH in the Fourier domain and Vérinaud [20] for the pyramid one). It is a $N_{gs} \times (2N_{gs})$ bloc diagonal matrix. Each bloc is a two-element column vector modeling one WFS. The upper element is the WFS operator along x, and the lower element is the WFS operator along y. Each WFS measures frequencies up to a cut-off frequency f_c^{WFS}. Beyond this cut-off frequency, the WFS operator is equal to 0. The $\mathbf{M}\mathbf{P}_\alpha^{\mathbf{L}}$ matrix describes the sensitivity of the system and will be referred as the global system interaction matrix.

Finally, $\mathbf{b}$ is a column vector of the noise associated with each GS (dimension $= 2N_{gs}$), which originates from photon and detector noises. This WFS measurement noise is statistically independent for distinct GS and x and y components. The variance associated with it is assumed to be identical for all frequencies associated with a given GS, with a value denoted as σ_i^2 (rd^2) for GS number i.

Finally, one still has to express $\tilde{\varphi}_{\mathbf{DM}}$. With linear assumptions, the most general form for the correction phases is a sum of suitably filtered measurements defined as

$$\varphi_{\mathbf{DM}} = \mathbf{W}\tilde{\phi}^{\mathbf{meas}}, \qquad (12)$$

where $\mathbf{W}$ is the phase volume reconstructor matrix of size $(2N_{gs}) \times N_{DM}$, which converts the $(2N_{gs})$ measurements

into N_{DM} correction phases. Fusco *et al.* [4] have shown that this matrix can be split in two independent matrices, written as

$$\mathbf{W} = \mathbf{P}_{\mathbf{opt}}\mathbf{W}_{\mathbf{tomo}}. \qquad (13)$$

The reconstruction can thus be seen as two consecutive steps. The first one, corresponding to $\mathbf{W}_{\mathbf{tomo}}$ (dimension $= 2N_{gs} \times N_L$), provides an estimate of the turbulent phases on each reconstructed turbulent layer; it is the tomographic reconstruction. It depends only on the GS configuration $\{\alpha_i\}$, and the atmospheric conditions. The second step, corresponding to $\mathbf{P}_{\mathbf{opt}}$ (dimension $= N_L \times N_{DM}$), consists of a projection of the tomographic solution onto the DMs. It is a geometrical operation that provides the correction phases on the DMs from the tomographic estimated phase in the volume. It depends on the size of the scientific FoV and on the number and positions of the DMs with respect to the reconstructed layers. In the following, we choose to investigate these two steps independently.

C. Phase Reconstruction: $\mathbf{W}_{\mathbf{tomo}}$
The goal of the tomographic reconstructor is to find the best possible estimate of the phase volume from noisy GS measurements. The phase volume estimate is written as

$$\hat{\tilde{\varphi}}_{\mathbf{turb}} = \mathbf{W}_{\mathbf{tomo}}\tilde{\phi}^{\mathbf{meas}}, \qquad (14)$$

where the hat stands for the volume estimates. The number of sources is limited, while the number of turbulent layers is large, not to say infinite, meaning that the problem is ill-conditioned and generally not directly invertible. Several methods have been proposed to reconstruct the turbulence volume. We choose to investigate three reconstructors that are frequently used and discussed: the minimum mean Square error (MMSE), the simple least square estimator (LSE) and the truncated LSE (TLSE) approach.

1. MMSE Reconstruction
The MMSE estimator minimizes the residual phase variance in each reconstructed layer following a quadratic criterion between actual and estimated phases

$$\sigma_{res}^2 = \langle \|\tilde{\varphi}_{\mathbf{turb}} - \mathbf{W}_{\mathbf{tomo}}(\mathbf{M}\mathbf{P}_\alpha^{\mathbf{L}} \tilde{\varphi}_{\mathbf{turb}} + \mathbf{b})\|^2 \rangle. \qquad (15)$$

In the Fourier domain, the derivation of Eq. (15) with respect to $\mathbf{W}_{\mathbf{tomo}}$ is done frequency by frequency. This leads to the optimal solution defined by

$$\mathbf{W}^{\mathbf{MMSE}} = [(\mathbf{M}\mathbf{P}_\alpha^{\mathbf{L}})^{\mathbf{T}}(\mathbf{C_b})^{-1}\mathbf{M}\mathbf{P}_\alpha^{\mathbf{L}} + \mathbf{C}_{\varphi_{\mathbf{n}}}^{-1}]^{-1}(\mathbf{M}\mathbf{P}_\alpha^{\mathbf{L}})^{\mathbf{T}}(\mathbf{C_b})^{-1},$$

$$\qquad (16)$$

which can also be written as [21]

$$\mathbf{W}^{\mathbf{MMSE}} = \mathbf{C}_{\varphi_{\mathbf{n}}}(\mathbf{M}\mathbf{P}_\alpha^{\mathbf{L}})^{\mathbf{T}}[\mathbf{M}\mathbf{P}_\alpha^{\mathbf{L}}\mathbf{C}_{\varphi_{\mathbf{n}}}(\mathbf{M}\mathbf{P}_\alpha^{\mathbf{L}})^{\mathbf{T}} + \mathbf{C_b}]^{-1}.$$

$$\qquad (16')$$

This reconstructor includes prior knowledge of the phase statistics and noise power spectrum by means of $\mathbf{C}_{\varphi_{\mathbf{n}}}$ and $\mathbf{C_b}$.

As the turbulent layers are independent, for each frequency, $\mathbf{C}_{\varphi_{\mathbf{n}}}$ is a diagonal matrix of size $N_L \times N_L$. The di-

agonal components are given by the fraction of turbulent energy associated with each layer: $\mathbf{C}_{\varphi_{\mathbf{n}}} = \mathrm{diag}(\lambda_1 C_\phi, \ldots, \lambda_{N_L} C_\phi)$.

WFS measurement noises are statistically independent for distinct GSs and orthogonal directions, meaning that $\mathbf{C_b}$ is a diagonal matrix of size $2N_{gs} \times 2N_{gs}$. The noise variance is identical for all the frequencies (white noise) with a value defined by $\sigma_{i,(x,y)}^2 (\mathrm{rd}^2)$ for the GS number i. It can be different for different GSs and for x and y directions: $\mathbf{C_b} \propto \mathrm{diag}(\sigma_{1,X}^2, \sigma_{1,Y}^2, \ldots, \sigma_{N_{gs},X}^2, \sigma_{N_{gs},Y}^2)$.

If we assume the same noise σ^2 for all GSs and x and y directions ($\mathbf{C_b} \propto \mathbf{Id}$), we can factorize this noise term in the first form of $\mathbf{W^{MMSE}}$, and rewrite Eq. (16) as

$$\mathbf{W^{MMSE}} = [(\mathbf{MP}_\alpha^\mathbf{L})^\mathbf{T} \mathbf{MP}_\alpha^\mathbf{L} + \sigma^2 \mathbf{C}_{\varphi_\mathbf{n}}^{-1}]^{-1} (\mathbf{MP}_\alpha^\mathbf{L})^\mathbf{T}. \quad (17)$$

This form produces the regularization term $\sigma^2 \mathbf{C}_{\varphi_\mathbf{n}}^{-1}$, which is none other than the inverse of the signal to noise ratio (SNR). We will see in Subsection 5.B the role of this regularization term in avoiding the noise amplification due to unseen frequencies.

2. (T)LSE Reconstruction
The LSE estimate $\hat{\tilde{\varphi}}_{turb}$ is the one providing the best fit to the measurements; it can be found by minimizing the following criterion:

$$\sigma_{res}^2 = \langle \| \phi_{mes} - \mathbf{MP}_\alpha^\mathbf{L} \mathbf{W_{tomo}} \phi_{mes} \|^2 \rangle. \quad (18)$$

The minimization of the above criteria with respect to $\mathbf{W_{tomo}}$ leads to the well-known solution

$$\mathbf{W^{LSE}} = [(\mathbf{MP}_\alpha^\mathbf{L})^\mathbf{T} \mathbf{MP}_\alpha^\mathbf{L}]^{-1} (\mathbf{MP}_\alpha^\mathbf{L})^\mathbf{T}. \quad (19)$$

It is well known and interesting to note that this LSE solution corresponds to the MMSE one introduced in Eq. (17) for which the regularization term have been canceled ($\sigma^2 \mathbf{C}_{\varphi_\mathbf{n}}^{-1}$ tends to 0).

For some frequencies, the $(\mathbf{MP}_\alpha^\mathbf{L})^\mathbf{T} \mathbf{MP}_\alpha^\mathbf{L}$ is not invertible or badly conditioned. For such frequencies, truncated singular value decomposition (TSVD) is used to truncate these singular values below a preselected threshold. For the truncated frequencies, $\mathbf{W^{LSE}} = 0$ and $\hat{\tilde{\varphi}}_n = 0$. The choice of threshold is made empirically by trying to find the best trade-off between the number of truncated frequencies and noise amplification. In simulation, it is relatively straightforward to find the optimal threshold with an exhaustive exploration of threshold levels. For each configuration, we compute the residual variance as described in Subsection 2.B for a set of threshold levels, the optimal threshold being the one that minimizes the residual variance. In real systems, when accounting for overheads during on-sky operations, it is not easy to scan the parameter space. Hence all the following results for the TLSE case should be taken as optimistic ones.

D. Model and Statistical Priors
A few particulars on the reconstructors are important at this point:

• First, the number/altitudes of the reconstructed layers can be different from the "real" number/altitudes of atmospheric layers as introduced in Eq. (3). The choice of the number/altitudes of reconstructed layers comes from our knowledge of the atmospheric conditions. If our description of the atmospheric model is partial or wrong, we will commit an error. We will refer to this error as the "model error."

• Second, the value of the statistical priors used in the MMSE reconstructor can be different from real noise and turbulence statistics. This misknowledge leads to an additional error that will refer as the "statistical error." The TLSE does not explicitly include priors on phase and noise statistics. However, the truncation level is predefined based on assumed models for system/atmospheric conditions. A statistical error then leads to badly tuned truncation.

We discuss the effect of the model errors in Section 6 and of the statistical errors in Section 7.

E. Projection onto DMs: $\mathbf{P_{opt}}$
The tomographic reconstruction is followed by an optimal projection of the volume estimation onto the DMs. This can be written as

$$\varphi_{\mathbf{DM}} = \mathbf{P_{opt}} \hat{\tilde{\varphi}}_{\mathbf{turb}}. \quad (20)$$

The filter that optimally projects the turbulence volume onto the DMs depends on FoV optimization directions $\beta = \{\beta_i\}$ and is defined by [3,4]

$$\mathbf{P_{opt}} = [\langle (\mathbf{P}_{\beta_\mathbf{j}}^{\mathbf{DM}} \mathbf{N})^\mathbf{T} \mathbf{P}_{\beta_\mathbf{j}}^{\mathbf{DM}} \mathbf{N} \rangle_\beta]^{-1} \langle (\mathbf{P}_{\beta_\mathbf{j}}^{\mathbf{DM}} \mathbf{N})^\mathbf{T} \mathbf{P}_{\beta_\mathbf{j}}^\mathbf{L} \rangle_\beta, \quad (21)$$

where, $\langle \ \rangle_\beta$ represents the average over all the N_{ang} directions. $\mathbf{N}$ is a diagonal matrix of sizes $N_{DM} \times N_{DM}$ defined by $\mathbf{N} = \mathrm{diag}(A_1, \ldots, A_{N_{DM}})$, with $A_n = 1$ when the considered frequency is smaller than the DM cut-off frequency and 0 otherwise. $\mathbf{P}_{\beta_j}^{\mathbf{DM}}$ and $\mathbf{P}_{\beta_j}^\mathbf{L}$ are constructed in the same way as $\mathbf{P}_\theta^{\mathbf{DM}}$ and $\mathbf{P}_\theta^\mathbf{L}$ in Eq. (10).

If the mirrors' positions exactly match the reconstructed layers, no projection is required and $\mathbf{P_{opt}} = \mathrm{Id}$. In such a situation there is no particular optimization in the FoV and no additional error due to projection. When the mirror positions do not match the turbulent layers, optimizing for a particular FoV position may degrade the cor-
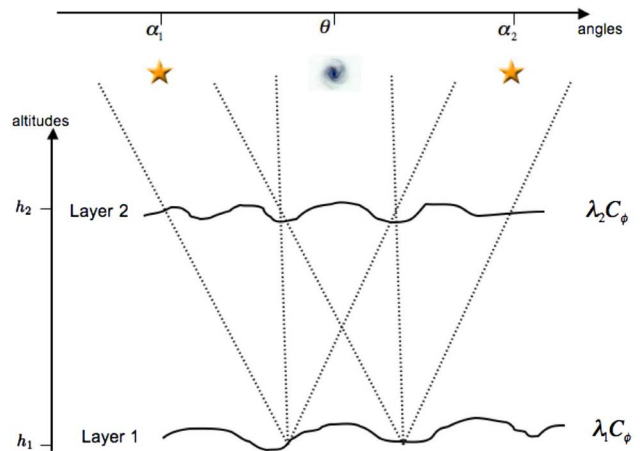

Fig. 2. (Color online) System geometry for the 2GS two-layer simple case. The altitude of layers is $h_1 = 0$ and $h_2 = h$. Two GSs are considered in directions α_1 and α_2, and the separation α_{12} between the GSs is 2 arcmin. Performance is evaluated at the center of the FoV: $\theta = 0$.

Table 1. Ten-Layer Turbulence Profile Altitudes and Relative Layer Strength

h_n (m)	0	200	600	1200	3000	4700	7300	8500	9700	11000
λ_n	0.41	0.16	0.1	0.09	0.08	0.05	0.045	0.035	0.02	0.01

rection in other directions. Trade-offs have to be made for a specific set of FoV positions, and the matrix $\mathbf{P_{opt}}$ performs these trade-offs optimally. In such a situation, an additional error term due to projection arises: the so-called generalized fitting. We discuss this term in Section 8.

F. Derivation of the Residual-Phase Power Spectrum
Putting Eqs. (10)–(12) into Eq. (6), we then have

$$\tilde{\phi}_\theta^{res} = \mathbf{P}_\theta^{\mathbf{L}}\tilde{\varphi}_{\mathbf{turb}} - \mathbf{P}_\theta^{\mathbf{DM}}\mathbf{W}(\mathbf{MP}_\alpha^{\mathbf{L}}\tilde{\varphi}_{\mathbf{turb}} + \mathbf{b}). \qquad (22)$$

We can now derive the residual PSD for each frequency. By definition, $\mathrm{PSD}_\theta^{res}$ is the statistical average of the square modulus of the residual phase $\tilde{\phi}_\theta^{res}$. Assuming that noise and phase are statistically independent of each other, it follows that
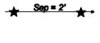
$$\mathrm{PSD}_\theta^{res} = (\mathbf{P}_\theta^{\mathbf{L}} - \mathbf{P}_\theta^{\mathbf{DM}}\mathbf{WMP}_\alpha^{\mathbf{L}})\mathbf{C}_{\varphi_{\mathbf{n}},\mathbf{t}}(\mathbf{P}_\theta^{\mathbf{L}} - \mathbf{P}_\theta^{\mathbf{DM}}\mathbf{WMP}_\alpha^{\mathbf{L}})^{\mathbf{T}}$$

$$+ (\mathbf{P}_\theta^{\mathbf{DM}}\mathbf{W})\mathbf{C}_{\mathbf{b},\mathbf{t}}(\mathbf{P}_\theta^{\mathbf{DM}}\mathbf{W})^{\mathbf{T}}. \qquad (23)$$

In the above equation, we have introduced $\mathbf{C}_{\varphi_{\mathbf{n}},\mathbf{t}}$, the power spectrum matrix of the phases in the turbulence volume, and $\mathbf{C}_{\mathbf{b},\mathbf{t}}$, the noise power spectrum matrix. These matrices stand for true noise/atmospheric statistical conditions. They are both diagonal matrices constructed in the same way as $\mathbf{C}_{\varphi_{\mathbf{n}}}$ and $\mathbf{C}_{\mathbf{b}}$ in Eq. (16). The differences from $\mathbf{C}_{\varphi_{\mathbf{n}}}$ and $\mathbf{C}_{\mathbf{b}}$ are that $\mathbf{C}_{\varphi_{\mathbf{n}},\mathbf{t}}$ can be larger than $\mathbf{C}_{\varphi_{\mathbf{n}}}$ if we commit a model error, and $\mathbf{C}_{\mathbf{b},\mathbf{t}}$ can have different values of noise variance if we commit a statistical error (see Subsection 3.D). We distinguish these matrices from the one introduced as priors in Subsection 3.C.1 with the subscript t. In all the following, $\mathrm{PSD}_\theta^{res}$ will be our working starting point. All the matrices required to construct $\mathrm{PSD}_\theta^{res}$ are also described in more detail in [7].

4. SIMULATION CONDITIONS
On the basis of the residual phase PSD derived in Subsection 3.F, we want now to investigate the different errors introduced in Section 1: unseen frequencies, model/statistical errors, and projection errors. For that we define three simulation cases representative of different GS/FoV configurations:

- The first case, called "2GS," is a simple one-dimensional model where the atmosphere is composed of only two layers. One of the two layers is located in the pupil, and the other one is at an altitude $h = 8$ km. We consider that the two layers have a relative turbulence strength profile defined by $[\lambda_1, \lambda_2]$. We consider two GSs separated by a distance $\alpha_{1,2} = 2$ arcmin. This simple configuration is used mainly to derive didactic examples, illustrated with the one-dimensional residual PSD. Figure 2 describes the geometry of this case.
- The second case, called "4GS," is a more realistic model where the atmosphere is composed of ten layers. The altitudes and strength of the layers are summarized in Table 1. This turbulence volume is sensed with 4GSs located on a 2-arcmin-diameter circle. All GS have the same noise variance $\sigma^2 = 0.5$ rd^2. This constellation is used as a representative configuration for a medium-FoV system.
- The third case, called "8GS," uses the same turbulence profile but is sensed with 8GSs located on a 5-arcmin-diameter circle. All GSs have the same noise variance $\sigma^2 = 0.5$ rd^2. This constellation is used as a representative configuration for a large-FoV system.

Table 2 summarizes the main parameters of these three simulation cases. For all simulation cases, the Fried parameter is set to $r_0 = 0.12$ m defined at 0.5 μm and $L_0 = 50$ m. We assume the that turbulence measurements are performed with a SH WFS. For that case, Rigaut *et al.* [14] show that the measurement operation, without aliasing and finite exposure time, can be modeled by a *M*

Table 2. Simulation Configurations

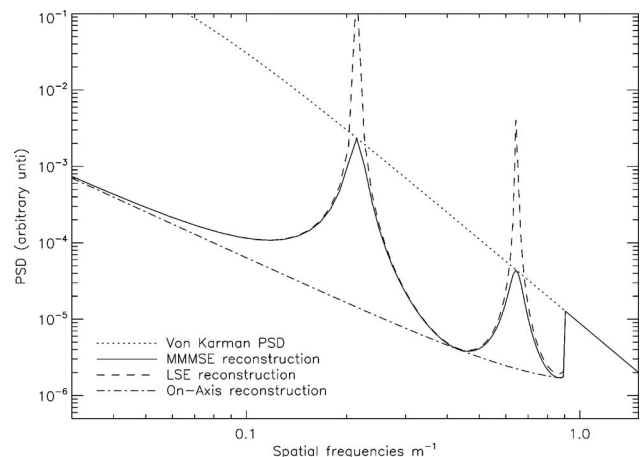|	2GS Config.	4GS Config.	8GS Config.
Atmos. Profile	2 Layers	10 Layers	10 Layers
Constellation	★ Sep = 2' ★	Sep = 2'	Sep = 5'
# GS	2	4	8
FoV Diameter	2'	2'	5'
Noise/GS	0.5 rd^2	0.5 rd^2	0.5 rd^2

Fig. 3.   Comparison of residual PSDs for the MMSE reconstruction (solid curve) and untruncated LSE reconstruction (dashed curve). Uncorrected Von-Kármán (dotted curve) and on-axis reconstruction (dashed–dotted curve) PSDs are also plotted for comparison. In this example, the two layers have the same turbulent strength and the WFS cut-off frequency is $f_c = 0.9$ m^{-1}. Two unseen frequencies appear for $f_1 = 0.215$ m^{-1} and $f_2 = 0.645$ m^{-1}, and two neutral frequencies appear for $f_1 = 0.43$ m^{-1} and $f_2 = 0.86$ m^{-1}.

$= 2j\pi f_{x,y}$ sinc$(\pi d f_{x,y})$ term, where we assumed a square geometry for subapertures with a size (reported in the telescope pupil) equal to d. For our example, we consider that all WFSs have the same subapertures sizes. This implies that all frequencies greater than $f_c = 1/2d$ are not measured. We further assume that all the GSs have the same noise variance defined by $\sigma^2 = 0.5$ rd^2, where σ^2 are the diagonal components of $\mathbf{C_{b,t}}$. Performance is evaluated at 1.65 μm (H Band) by projecting the volumetric residual phase in the direction of interest θ. Unless specified otherwise, it is evaluated at the center of the FoV ($\theta = 0$).

In the following sections, we make use of the above three simulation cases to investigate (i) pure tomographic reconstruction in Section 5, (ii) model/statistical errors in Sections 6 and 7, and (iii) projection issues in Section 8. We want to emphasize that most of these errors depend strongly on the turbulence profile. More precisely, we will see that for a given isoplanatic angle, the relevant parameter is defined by the product of layer altitudes and GS separations: $h_n\alpha$. In our analysis, we have chosen to fix

the turbulence profile and investigate these errors in term of GS separation (FoV). Numerical results presented in the following should then not be seen as absolute results but rather as quantitative insights used to illustrate general trends.

5. PURE TOMOGRAPHIC RECONSTRUCTION

In this section, we consider the ideal situation where noise and turbulence conditions are perfectly known: $\mathbf{C_{\varphi_n}}$ and $\mathbf{C_b}$ used in Eq. (16) are then identical to $\mathbf{C_{\varphi_n,t}}$ and $\mathbf{C_{b,t}}$ used in Eq. (23). This situation is generally called the "pure tomographic reconstruction."

A. Analytical Expressions of the Residual PSD
We first consider the 2GS case. From this simple one-dimensional configuration, we can derive the analytical form of the residual phase PSD for both filters. Equation (23) can be written when considering a (T)LSE as

$$\mathrm{PSD}^{res}_{\theta=0} = \begin{cases} \dfrac{\sigma^2[2 - \cos(2\pi f(\alpha_1 - \theta)h) - \cos(2\pi f(\alpha_2 - \theta)h)]}{2\sin^2(\pi f\alpha_{12}h)M^2} & \text{for } f < f_c \text{ and for nontruncated frequencies} \\ C_\phi & \text{for } f \geq f_c \text{ or for truncated frequencies} \end{cases}, \quad (24)$$

while with an MMSE, it reads

$$\mathrm{PSD}^{res}_{\theta=0} = \begin{cases} C_\phi\left\{\dfrac{2MC_\phi\lambda_1\lambda_2\sigma^2[2 - \cos(2\pi f(\alpha_1 - \theta)h) - \cos(2\pi f(\alpha_2 - \theta)h)] + \sigma^4}{4\sin^2(\pi f\alpha_{12}h)M^4C_\phi^2\lambda_1\lambda_2 + 2M^2\sigma^2C_\phi + \sigma^4}\right\} & \text{for } f < f_c \\ C_\phi & \text{for } f \geq f_c \end{cases}. \quad (25)$$

In Fig. 3 we compare these two one-dimensional residual PSD laws for $\theta = 0$ as well as the uncorrected Von-Kármán spectrum and the on-axis reconstruction for comparison. The on-axis reconstruction corresponds to a classical LSE single conjugated AO configuration and is computed by setting the two GSs in the direction of interest. It follows the typical f^{-2} law expected for derivative WFS [22]. Since the two GSs are on-axis, we benefit from the global flux.

B. Notion of Unseen Frequencies and Neutral Frequencies
In Fig. 3, it appears that for some specific frequencies, the tomographic residual PSDs (either MMSE or LSE) diverge from the on-axis noise propagation, while other frequencies follow the on-axis noise propagation. To understand the behavior of these PSDs, we first consider the LSE reconstructor. From Eq. (24), we learn that the reconstruction error tends to infinity for each spatial frequency equal to $p/(\alpha_{12}h)$, where p is an integer. Indeed, each time the period of a frequency exactly matches the GS separation, the sum of the phase perturbations induced by the two layers is exactly zero and the phase information for these frequencies is lost. We refer to these

frequencies as "unseen frequencies," as they are not sensed by the WFSs. For a given turbulence profile, the unseen frequencies depend only on the GS positions: the more distant the GSs, the smaller the spatial frequencies affected and the larger the number of unseen frequencies in a given frequency range of interest. The GS separation can then be understood as a spatial basis that sets the sensitivity of the filter to the different frequencies.

We now investigate the effect of the unseen frequencies when looking in a particular direction of interest θ. This effect relies on the numerator of Eq. (24). We find that for some specific frequencies this numerator goes to zero. This happens each time the sum of the phase perturbations induced by the two layers is exactly zero in the direction θ. These frequencies do not affect the performance in the direction of interest; we will call them "neutral frequencies." For instance, when the direction of interest is at $\theta = 0$ (as in Fig. 3), each of these neutral frequencies occurs as $f = 2p/(\alpha_{12}h)$. Therefore, for this specific direction, the neutral frequencies cancel one out of every two unseen frequencies. We note that for the frequency that exactly corresponds to both an unseen and a neutral frequency, Eq. (24) is undetermined. For that specific frequency, calculation of the limits gives

$$\text{PSD}_{\theta=0}^{res} = \left(\frac{\sigma^2}{2M^2} \right), \tag{26}$$

which is the classical on-axis propagation law [14].

Another example of the effect of the neutral frequencies is when the direction of interest lies exactly on one of the GSs (e.g., $\theta = \alpha_1$). In such a situation all the unseen frequencies are canceled by the neutral frequencies: an unseen frequency has no effect on the image quality in the GS directions.

For the pure LSE reconstructor, unseen frequencies are a real issue, as they lead to an overamplification of noise. For these frequencies, the interaction matrix coefficients go to zero, the direct inverse is ill-conditioned and the noise is dramatically amplified. Around an unseen frequency, there is a set of badly-seen frequencies. For these frequencies, measurement is close to zero, but since the WFSs are noisy, the same problem as for the unseen frequencies applies. In the following, we will also refer to these frequencies as unseen frequencies.

To avoid this noise amplification, one should use the TLSE reconstruction. In Fig. 4 we show the corresponding residual PSD for the TLSE reconstructor that has the best threshold. Noise amplification is avoided, at the price of uncorrected frequencies.

In contrast to the TLSE reconstructor, the MMSE reconstructor does not require any truncation. In fact, the MMSE filter includes prior knowledge of the SNR by the mean of the regularization term $\sigma^2 \mathbf{C}_{\varphi_{\mathbf{n}}}^{-1}$ [see Eq. (17)]. This regularization appears as an additive term in the numerator of Eq. (25), which weights the noise propagation. Thanks to this regularization term, the MMSE is able to optimize the reconstruction depending on the SNR: for frequencies that have a good SNR, the MMSE and TLSE are equivalent; for poor-SNR frequencies, the inverse of the interaction matrix is weighted by the regularization term, avoiding noise amplification. It follows that (i) even on a pure unseen frequency, the residual MMSE PSD is never higher than the C_ϕ signal variance and (ii) whatever the truncation threshold used for the TLSE estimator, the MMSE approach always gives smaller residual variance (see also [4]). Following with the MMSE, it is in-

teresting to note that for a frequency exactly on an unseen mode, the residual PSD is written as

$$\text{PSD}_{\theta=0}^{res} = C_\phi \left(\frac{8M^2 C_\phi \lambda_1 \lambda_2 + \sigma^2}{2M^2 C_\phi + \sigma^2} \right). \tag{27}$$

Equation (27) indicates that when the turbulence is equally distributed between the two layers ($\lambda_1 = \lambda_2 = 0.5$), the residual PSD exactly reaches the uncorrected spectrum. However, as long as the turbulence strength profile is not uniformly distributed, the residual error is always lower than the uncorrected spectrum. We illustrate this behavior in Fig. 5 with three residual PSDs computed for, respectively (from top to bottom), [$\lambda_1 = 0.5$, $\lambda_2 = 0.5$], [$\lambda_1 = 0.7$, $\lambda_2 = 0.3$], and [$\lambda_1 = 0.9$, $\lambda_2 = 0.1$] (the [$\lambda_1 = 1$, $\lambda_2 = 0$] case is superimposed on the on-axis reconstruction error). This behavior can be explained by the fact that when the turbulence is equally distributed, the chance that the sum of the two layers will give a null measurement is maximal. Statistically, no information can be extracted from the measurement. When the two layers do not have the same strength, this probability decreases, and even for an unseen frequency, some signal can be measured. As a limiting configuration, if one layer is free of turbulence ($\lambda_{1,2} = 0$), we are able thanks to this prior information to entirely recover the incoming perturbation. As the MMSE filter includes the knowledge of turbulence strength per layer, it is able to discriminate these conditions and to modulate the regularization term layer per layer. This also illustrates how the prior knowledge of the statistical conditions can consequently reduce the residual variance more than the crude TLSE approach.

C. Generalization to Realistic Cases

To understand the effect of a larger number of layers/GSs on unseen frequencies, we first start with a generalization of the simple 2GS case. In Fig. 6 we show the residual PSD for the 2GS case but treated as a two-dimensional configuration. On the left, we keep the two-layer atmosphere, whereas on the right we use the ten-layer profile as defined in Table 1. We display here only the results of the MMSE reconstructor. Note that a cut along the *x* coordinate on the left PSD of Fig. 6 would give the same MMSE reconstructor plot as the one presented in Fig. 3.
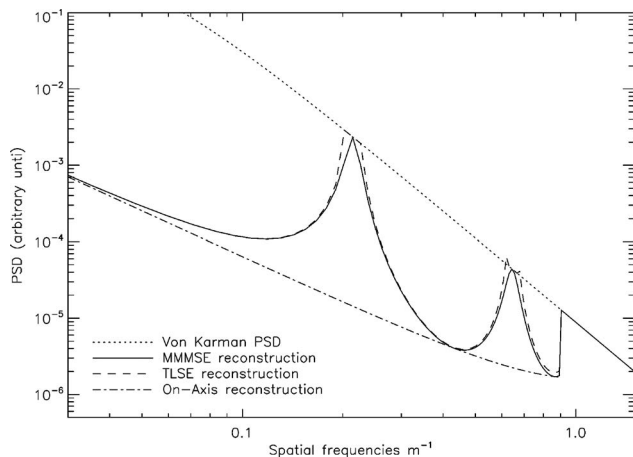

Fig. 4.   Same as Fig. 3 with the TLSE reconstructor. The threshold was optimized to minimize the residual variance.
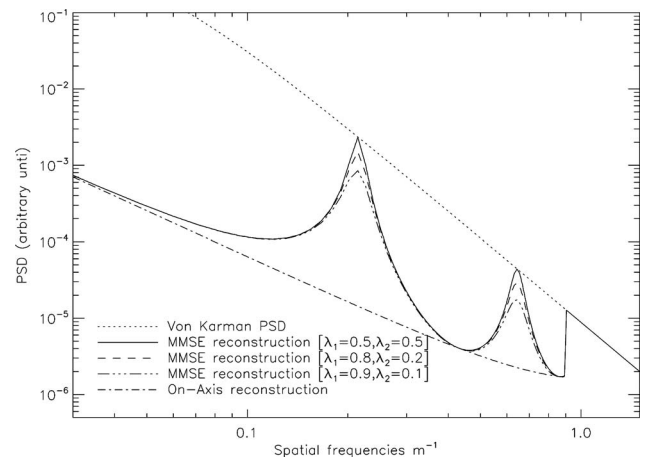

Fig. 5.   Influence of turbulence strength distribution on MMSE reconstruction error.
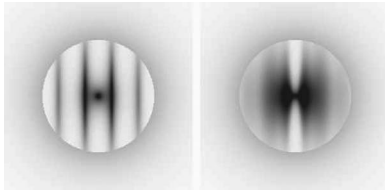
Fig. 6. Two-dimensional residual PSDs for the 2GS constellation with the two-layer profile (left) and the ten-layer profile (right). Log scale and inverted colors are used. The GS orientation is the same as in Table 2.

If we compare the shape of the two PSDs presented in Fig. 6, we can easily understand the effect of multiplying the number of layers: unseen frequencies become sectors instead of localized energy peaks. Indeed, with several layers, each pair of turbulent layers creates its own set of unseen frequencies, so the energy is spread out over more frequencies.

The second important point to emphasize is that unseen frequencies appear in only the parallel direction of the GS geometry. As explained by Tokovinin and Viard [9], for all the frequencies perpendicular to the GS direction ($f = \{f_x = 0; f_y\}$ for the 2GS case), the effective separation between the GSs in each layer ($\alpha_{1,2} h_n$) will not change the measured phase of those frequencies. These frequencies are always perfectly measured; the noise propagation is the one of the classical AO situations. This explains the "clean" frequency area along the y coordinate in Fig. 6. The width of this clean frequency area depends only on the GS separation that dictates the lowest unseen frequency.

We are now able to understand the generalization to the 4GS–8GS cases. In Fig. 7, we show the two-dimensional residual PSDs for the MMSE (left), the TLSE (center), and the LSE (right) for the 4GS (top) and 8GS (bottom) constellations. The 4GS case is none other than the product of two 2GS constellations rotated by 90°. We retrieve two clean frequency areas oriented toward the GS directions. The same argument can be applied to the 8GS constellation. In addition, the diameter of the 8GS constellation is larger than the 4GS one: the width of its clean frequency area is smaller. In Fig. 7, it also appears that the variance is much higher for LSE or TLSE reconstructors than for the optimal MMSE one, as already explained for the 2GS case in Fig. 4.

Finally, we note that as expected the number of low frequencies affected by unseen modes is larger for the large-
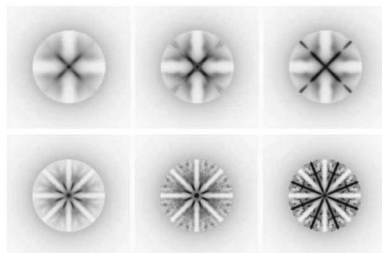

Fig. 7. Two-dimensional residual PSDs for the 4GS (top) and 8GS (bottom) cases. From left to right: MMSE, TLSE, and non-truncated LSE. Log scale and inverted colors are used. All PSDs are displayed with same scale. The GSs' orientation are the same orientation as in Table 2.

FoV configuration (the 8GS case) than in the 4GS configuration. The noise level associated with each frequency is, however, lower because twice as many GSs are used. The result is that the 4GS and the 8GS configurations give similar residual variances for the MMSE reconstruction: ~0.77 rd^2 (with our simulation conditions).

6. MODEL ERRORS

Up to now, we have assumed that the priors were perfectly tuned, i.e., that they do correspond to real conditions. These priors come from our knowledge of the system/atmospheric conditions and are not always easily accessible. Moreover, they can evolve during an observation run, and it could be impractical to recompute the reconstruction matrix frequently. In any case, it is of prime importance to understand and quantify the effect of these statistical/model errors on the reconstruction process.

Still using the three configurations presented in Section 4, we first investigate the model errors with an error on the altitudes of the reconstructed layers and an error on the number of reconstructed layers. These errors occur in both the TLSE and the MMSE reconstructors. We then aim to (i) understand the effect of the model errors illustrated with the 2GS case; (ii) compare the relative performance and robustness of the TLSE and MMSE reconstructors with the 4GS configuration, and (iii) compare the medium- (4GS) and large-FoV (8GS) systems in the MMSE approach.

A. Error on Layer Altitude
We first start with the one-dimensional 2GS case. We recall that only two layers are considered in this case. In Fig. 8 we show an example for which (i) the upper reconstructed layer is higher than real layer (top panel) and (ii) the upper reconstructed layer is lower than real layer altitude (bottom panel). In both situations the residual PSD is strongly affected, and for some frequencies the residual variance rises above the uncorrected PSD.

An error on the altitude where the layers are reconstructed affects the frequencies where unseen modes should be regularized/truncated. In fact, the altitudes of the reconstructed layers introduced in the model set the sensitivity of the reconstructors to unseen frequencies. A wrong geometry implies that wrong modes are going to be regularized/truncated. For the frequencies that correspond to well-seen frequencies for the model, the direct inverse of the interaction matrix is performed, whereas these frequencies could correspond to badly seen modes in the real geometry. For these frequencies, an overamplification of noise could appear. Conversely, some frequencies that are well seen by the real geometry could be treated as unseen frequencies by the model. For these modes, whereas a direct inverse would have worked well, over-regularization or truncation limits the accuracy of the reconstruction.

In a more realistic configuration, the atmosphere includes several dominant layers, and this error will be minimized. Of course, the best match between real profile and dominant layers will give the best results. To illustrate this point, we investigate our realistic ten-layer cases (4GS–8GS). We reconstruct the ten layers, but for
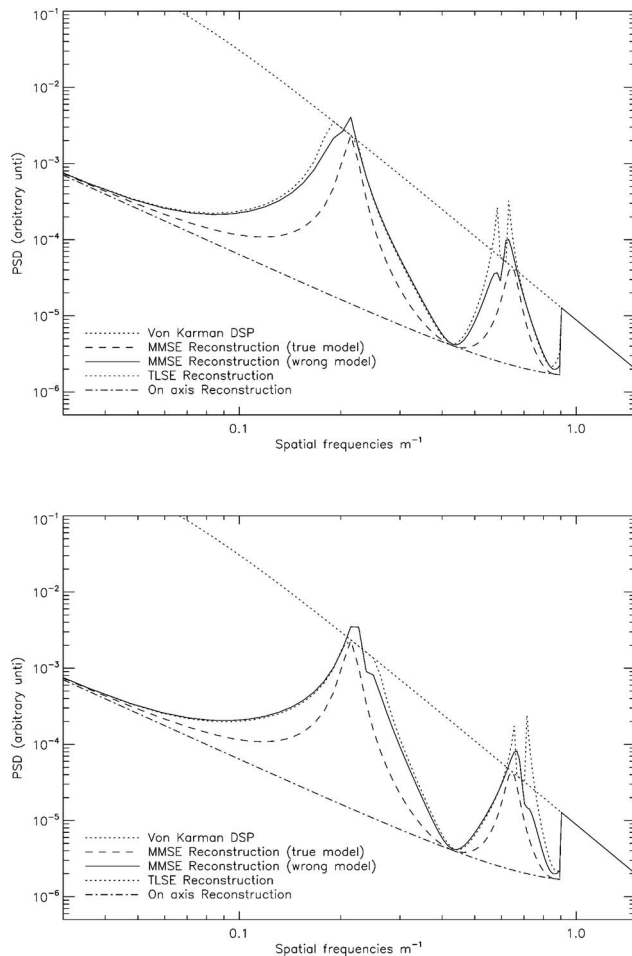
Fig. 8.   Residual PSD for an error in the altitude of the reconstructed layer. Top, upper altitude is overestimated (8.5 km instead of 8 km). Bottom, upper altitude is underestimated (7.5 km instead of 8 km).

each reconstructed layer we allow an error in altitude of $\pm X\%$, X going from 0% to 50%. For each altitude error, we perform 50 random trials and compute the mean residual variance. Results are shown in Fig. 9.

We first compare the results obtained for the 4GS case. We find that the two reconstructors (MMSE and TLSE)
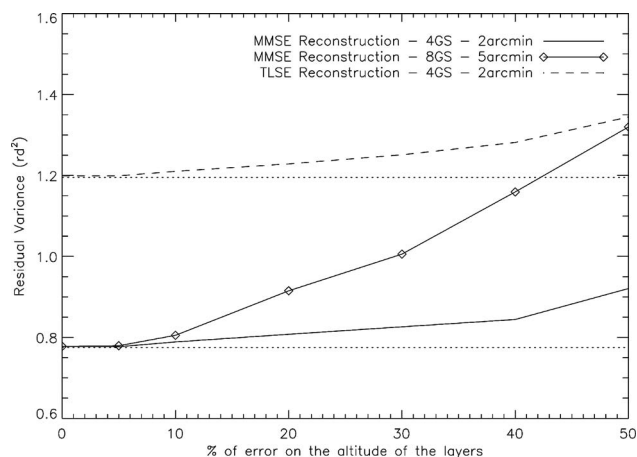
Fig. 9.   Ten-layer profile. Effect of an error on the reconstructed altitudes of each layer. "% of error" means that each reconstructed layer is at an altitude of $H \pm HX\%$.

follow the same tendency: the residual variance increases with the error on the model altitude. In addition, the order of magnitude of this error is more or less the same for both reconstructors.

If we now compare the results of the 4GS and 8GS cases, we notice that the large-FoV 8GS configuration is much more sensitive to an error on layer altitudes than the medium-FoV 4GS one. For the medium-FoV configuration, the effect of this error is moderated: an error of 50% on the layer altitudes increases the residual variance by $\sim 20\%$ with our turbulence profile. This indicates that a perfect knowledge of layer altitude is not necessary as long as many layers are reconstructed. However, this is no longer true for the large-FoV configuration: an error of 50% increases the residual variance by almost a factor of 2. In analogy to what is explained by Ragazzoni [23], the larger the distance between reconstructed and true layer, the lower the maximum equivalent frequency reconstructed in the true layer; and this maximal equivalent cut-off frequency depends on the FoV. This can also be explained with Fig. 7: when the FoV is increased, the unseen frequencies cover a larger area and the noise amplification affects more and more frequencies.

We conclude that this error term affects the tomographic reconstruction for large-FoV configurations and that either a good knowledge of the turbulence profile or the use of more GSs to reduce the unseen-frequencies area is required to limit the effect of this model error.

B. Error on Number of Layers

For computation reasons, the reconstruction is performed on a limited number of layers, generally smaller than in real turbulence conditions. In that configuration, the reconstructed volume does not match the real profile, and the resulting error can be significant. We first illustrate the effect of an incorrect number of reconstructed layers with the 2GS case. As only two layers are used to model the real turbulence profile, a single layer is used in the reconstruction. In Fig. 10, we illustrate this situation when the reconstructed layer is in the telescope pupil (solid curve) and when it is at an altitude of 4 km
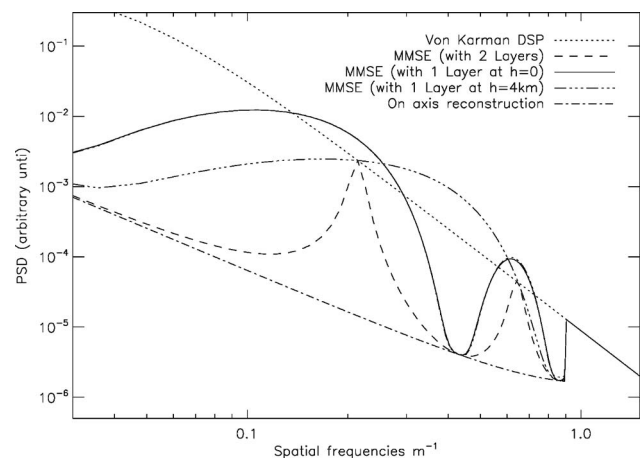

Fig. 10.   Residual PSD for a model error in the number of layers. The real profile is made of two layers, whereas the reconstruction model uses only one layer either in the telescope pupil (solid curve) or at an altitude of 4 km (dashed–dotted curve). The MMSE and TLSE cases are superimposed.
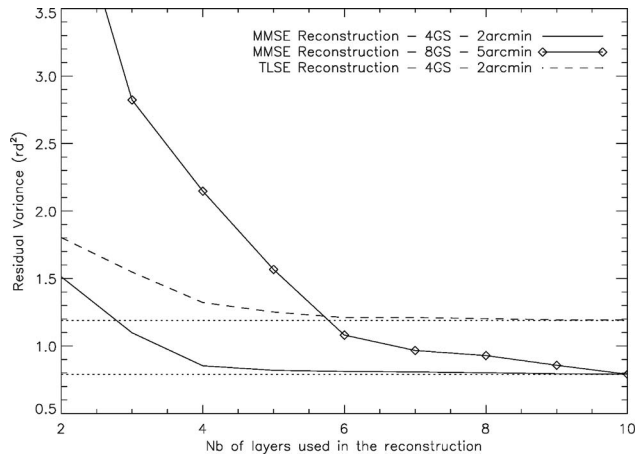
Fig. 11. Influence of the number of layers used in the reconstruction process. The real profile is the ten layers.

(dashed–dotted curve). It appears that the residual PSD is strongly influenced by this model error: the frequency domain affected by noise amplification is significantly enlarged. Interestingly, when the reconstructed layer falls just between the two real layers, this noise amplification is reduced compared with a reconstruction in the telescope pupil. Indeed, we can show that if the real turbulence is equally distributed between the two layers, the optimal altitude for the reconstructed layer is just at the middle. If the real turbulence is not equally distributed, the optimal altitude for reconstruction moves toward the strongest layer.

We now investigate the effect of this model error in presence of a "real" turbulence profile. To do so, we use the 4GS/8GS case, the real turbulence profile is defined by the ten-layer one, and we progressively increase the number of reconstructed layers. This procedure has been introduced by Fusco *et al.* [11] as equivalent layers (ELs). We then follow their approach for the definition of the altitudes/strength of the EL: the true profile is divided into N_{el} regularly spaced slabs, and for each slab an equivalent height and strength is computed. Results are shown in Fig. 11. This figure shows that for the medium-FoV constellation (4GS), a reconstruction on only a few layers (typically three or four) is enough to reduce the remaining error. With the 4GS case, we also find that the MMSE residual variance converges more rapidly than that of the TLSE. For the large-FoV configuration (8GS), we observe that at least eight layers must be reconstructed, and this number would certainly be larger if the initial profile had included more layers. The tomographic reconstruction is very sensitive to a model error on layer altitudes, particularly when the size of the FoV increases. We draw conclusions similar to those of Subsection 6.A: if the number of GS is limited, a good knowledge of the turbulence profile is necessary for an accurate reconstruction.

7. STATISTICAL ERRORS

In the previous section we have seen the effect of the model errors; we now investigate the effect of the statistical errors. We then assume that the model is perfectly

known: that we always reconstruct the real number/altitudes of the layers. Instead, we explore the consequences of (i) an error on the noise level ($\mathbf{C_b} \neq \mathbf{C_{b,t}}$), (ii) an error on the global strength of the turbulence ($r_0 \neq r_{0,t}$), and (iii) an error on the relative distribution of the turbulence ($\lambda_n \neq \lambda_{n,t}$).

An error on these statistical parameters will have an effect on the value of the SNR used by the model [see Eq. (17)]. Basically, the SNR used by the model sets the number of filtered/truncated frequencies. If this SNR is overestimated, the number of filtered/truncated frequencies decreases. For unseen frequencies, the model assumes that the SNR is good, a direct inversion of the interaction matrix is performed, and then we expect an overamplification of the noise localized on unseen frequencies. On the other hand, if the SNR is underestimated, the weight of the regularization term is increased: too many frequencies are filtered/truncated, whereas they could have been corrected. We then expect a broadening of the PSD around the unseen frequencies but no noise overamplification.

A. Error on Noise Priors
In Fig. 12, we first use the 2GS case to illustrate the effect of an error on the noise estimation. The top plot in Fig. 12
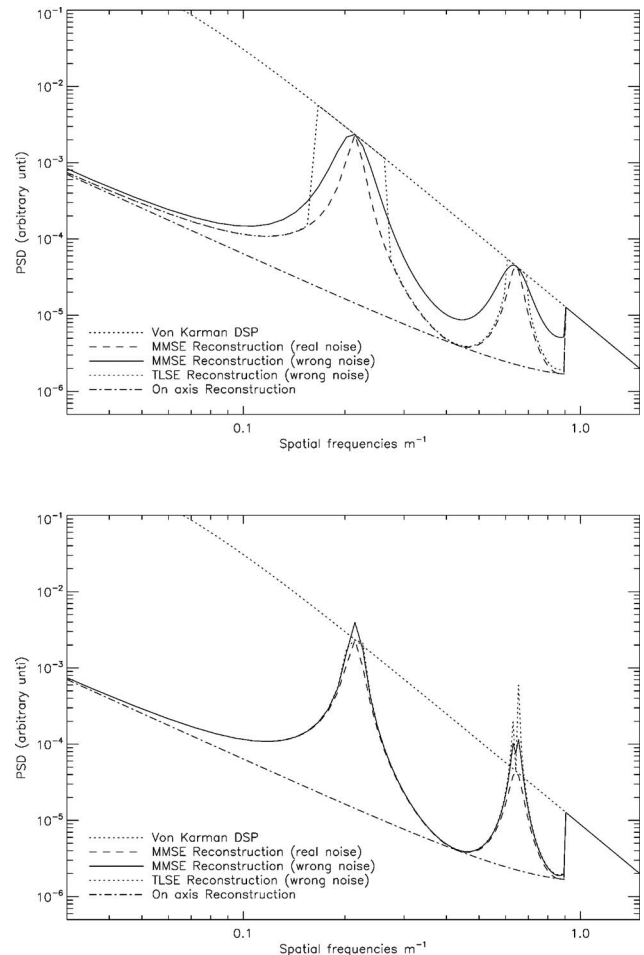

Fig. 12. Residual phase PSD for an error in noise priors. Top, overestimation of noise by a factor of 10: $\mathbf{C_b} = 10\mathbf{C_{b,t}}$. Bottom, underestimation of noise by a factor of 10: $\mathbf{C_b} = \mathbf{C_{b,t}}/10$.

shows the effect of an overestimation of the noise variance by a factor of 10 ($\mathbf{C_b} = 10\mathbf{C_{b,t}}$) and the bottom plot the effect of an underestimation of the noise variance by a factor of 10 ($\mathbf{C_b} = \mathbf{C_{b,t}}/10$). With this simple example, we indeed find that if the noise is overestimated (top figure), the residual PSD tends too rapidly to the uncorrected spectrum and too many frequencies are filtered/truncated. If the noise is underestimated (bottom figure), an overamplification of the residual error appears on the unseen frequencies and not enough frequencies are filtered/truncated.

Although the residual PSDs are affected by a wrong noise model, at first glance the effect of an error in the noise statistics does not seem to increase the residual error significantly. To quantify this effect, we use our realistic cases (4GS–8GS), and we plot in Fig. 13 the residual variance for a MMSE/TLSE reconstructor having wrong noise priors. The error in noise priors is given in percent of real noise: for instance, ±50% of error in noise variance corresponds to $\mathbf{C_b} = \pm 1.5 \mathbf{C_{b,t}}$. From Fig. 13, we learn the following:

- The residual variance in the MMSE approach is always smaller than that of the TLSE, which means that even with wrong priors, the MMSE reconstructor gives better results than that of the TLSE.
- The TLSE reconstructor is slightly more sensitive to noise error than that of the MMSE.
- The large-FoV configuration (8GS) is slightly more sensitive than that of the medium-FoV (4GS).
- For both reconstructors, if the noise level is not perfectly known, a conservative approach would be to overestimate the noise priors.

Another way to test the robustness of these reconstructors to the noise statistical error is to study, for a given reconstructor computed with a reference noise level, the effect on the performance when real conditions are changing. This is illustrated in Fig. 14 for the 4GS configuration. Both MMSE and TLSE reconstructors are computed for a given reference noise level ("variation for real noise variance"=0), and we compute the residual variances
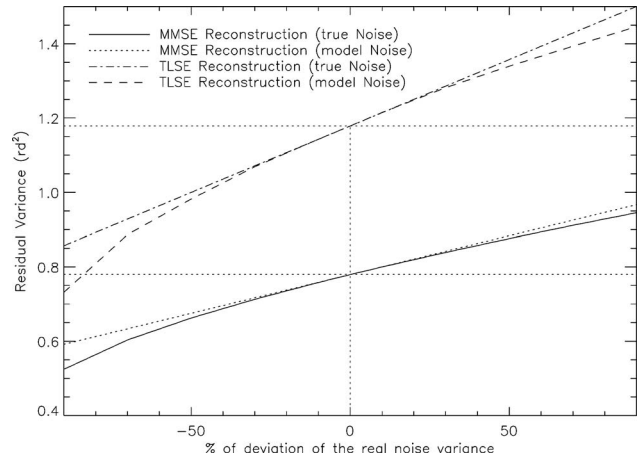
Fig. 14. Robustness of the MMSE/TLSE reconstructor to changes of "real" conditions. The "real" noise level (defined by $\mathbf{C_{b,t}}$) ranges from −90% to +90% around a reference level (0.5 $\mathrm{rd^2}$ when "% of deviation of the real noise variance" =0). The solid and dashed curves show the residual variance for perfectly tuned MMSE and TLSE reconstructors: noise priors follow the real noise variations. Dotted and dotted–dashed curves show the residual variance when noise priors are set to the reference noise level.

when real noise conditions are changing. The change in real noise variance is given in percent of noise priors: for example, ±50% of variation in real noise variance corresponds to $\mathbf{C_{b,t}} = \pm 1.5 \mathbf{C_b}$. In that situation, we find that the variation of the performance due to real conditions has a much greater effect on the residual variance than does the noise model error itself. Indeed, an increase in the real noise variance by 50% leads to an increase in the residual variance by $\sim 10\%$, whereas the corresponding model error increases the residual variance by only $\sim 3\%$ with our parameter set. Results for the 8GS configuration are very similar.

Combining the results of Fig. 13 and Fig. 14, we conclude that perfect knowledge of the noise priors is not required to obtain an accurate tomographic phase reconstruction.

B. Error on Turbulence Strength Priors

1. Error on r_0

The global strength of the turbulence r_0 is included in the estimation of the SNR. The conclusions drawn in the previous section are then exactly transposable here: (i) the MMSE is always better than the TLSE with wrong truncation threshold (ii), the large-FoV configuration is slightly more sensitive than the medium-FoV one, and (iii) a conservative approach would be to underestimate the global strength of the turbulence.

2. Error on Turbulence Strength per Layer

The turbulence strength distribution is another essential parameter to be introduced in the regularization process. This term affects only the MMSE reconstructor, as that of the TLSE does not include the profile distribution information. We have seen in Subsection 5.B that the turbulence strength distribution (λ_n) sets the SNR per layer. An
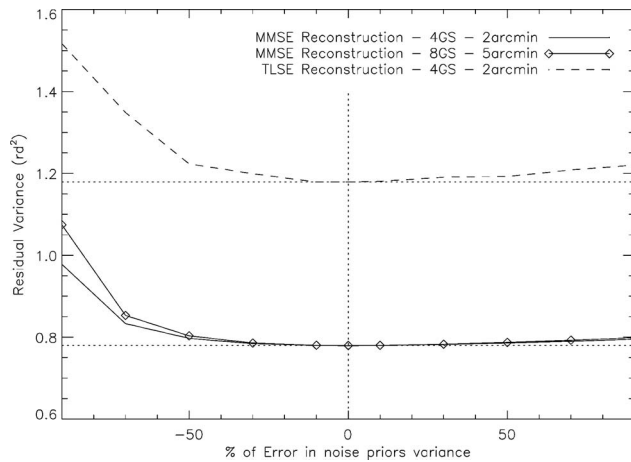

Fig. 13. Residual variance of the MMSE (solid curves) and TLSE (dashed curve) reconstructors with wrong noise model. Error in noise are given in percent of real noise. Dotted lines symbolize the minimal variance level when no errors on noise priors are committed.

error on the distribution of the turbulence strength will then produce an error on the SNR and an overamplification of noise.

We illustrate this point in Fig. 15 (top) with a pessimistic example: the turbulence strength distribution used by the model is [λ_1=0.1, λ_2=0.9], whereas the real turbulence distribution is [$\lambda_{1,t}$=0.9, $\lambda_{2,t}$=0.1]. For this pessimistic situation, we see in Fig. 15 that the residual PSD rises above the uncorrected turbulence PSD.

To avoid any noise amplification, a conservative approach would be to feed the model with a uniform turbulence strength distribution. This example is illustrated in Fig. 15 (bottom). The true turbulence distribution is still [$\lambda_{1,t}$=0.9, $\lambda_{2,t}$=0.1]; the one used by the model is [λ_1=0.5, λ_2=0.5]. With such a model, we have seen with Eq. (27) that the residual PSD becomes independent of the modeled strength distribution. As expected, the constant profile is the one providing the least information. With the conditions of Fig. 15 (top), the total variance of the MMSE is higher than that of the TLSE. However, following the conservative approach, i.e., the constant profile [Fig. 15 (bottom)], the MMSE is always better than the best-tuned TLSE.
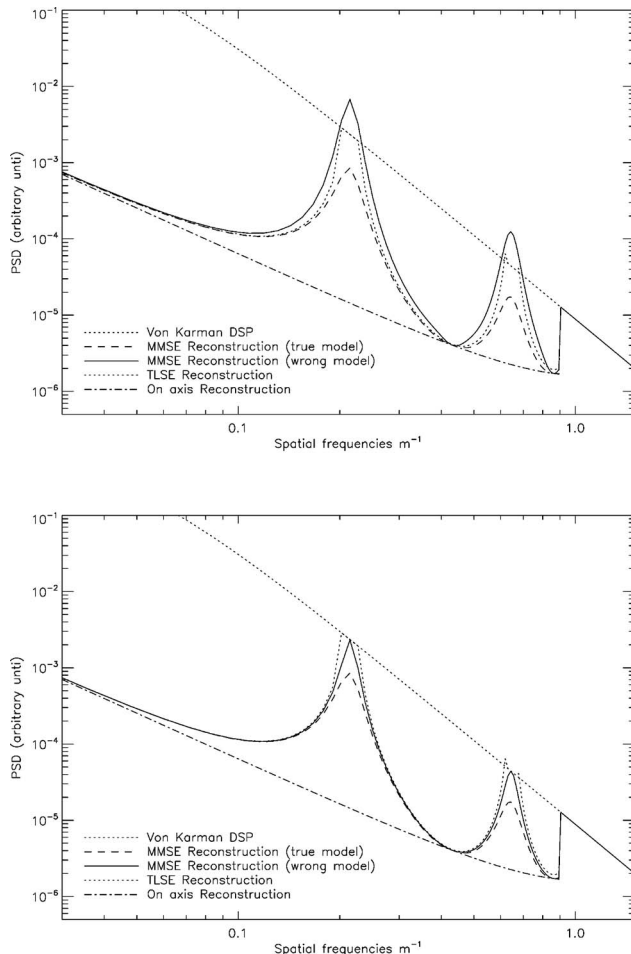

Fig. 15.   Error on turbulence strength priors with real turbulence distribution defined by [$\lambda_{1,t}$=0.9, $\lambda_{2,t}$=0.1]. Top, turbulence strength distribution used by the model is [λ_1=0.1, λ_2=0.9] (solid curve). For comparison, we plot the residual PSD if the model were correct (dashed curve). Bottom, turbulence strength distribution used by the model is [λ_1=0.5, λ_2=0.5].

We could further investigate these model/statistical errors, for instance by combining several terms. In that case, it is interesting to show that some model errors can be compensated by others (see, e.g., [24]). For example, the global variance due to a misknowledge of layer altitude could be compensated by using more noise priors in the reconstruction. A pure quantitative study of model errors depends on system characteristics, and this exhaustive and specific work is certainly beyond scope of this paper. Instead, in the next section we choose to investigate the error due to the projection onto DMs.

8. PROJECTION ONTO DMs

Up to now, we have considered only the tomographic phase reconstruction issue. In this section, we investigate the projection onto DMs and the supplementary error term related to generalized fitting. This term relies on Eq. (21) and depends on the optimization positions ({β_j}) and the number/altitudes of DMs. We use mainly the 4GS constellation, and we investigate different WFAO systems for a 42 m telescope. First we consider a projection onto a single DM with one direction of optimization (MOAO/LTAO), then we increase the optimization field still assuming a single DM (GLAO), and finally we introduce several DMs with an optimization in the field (MCAO).

Complementary to what has been done in the previous sections, we now extend the analysis to the whole field instead of concentrating on a particular direction. For each configuration, we choose to evaluate the performance in term of SR in 169 directions regularly spaced on a 13 × 13 grid across the field. Note that the SR metric is particularly relevant for diffraction-limited imagery (MOAO/LTAO/MCAO) but is less appropriate for partial atmospheric corrections (GLAO; e.g., [25]). Nevertheless, for the sake of clarity and simplicity, we have decided to consider only SR in the following.

For MOAO, optimization is done at the center of the field; for GLAO/MCAO, optimization is done on the same directions. Figure 16 illustrates the geometry used for the MOAO/LTAO configuration (top) and for the GLAO/MCAO configurations (bottom). Note that the GS constellation is rotated by 45° compared with Table 2.

In all of the following, except in Subsection 8.C.3, no model/statistical errors are introduced. We further assume that DM pitches match WFS pitches, which would correspond to DMs with ∼75 × 75 actuators. Atmospheric parameters are those introduced in Section 4. We stress that a different set of atmospheric parameters would lead to different numerical results. The derived performance is then indicative and useful only for a relative comparison of the systems. Finally, we recall that the telescope diameter is set to 42 m.

A. MOAO/LTAO: No Projection Error
For some specific observations a uniform correction of the whole FoV is not required. For instance, in three-dimensional spectroscopy extra-galactic studies, only a few directions of interest must be corrected for. This can be achieved by means of MOAO or LTAO ([26,27]). In these concepts, several GSs spread over the field are used to perform the tomographic reconstruction of the turbu-
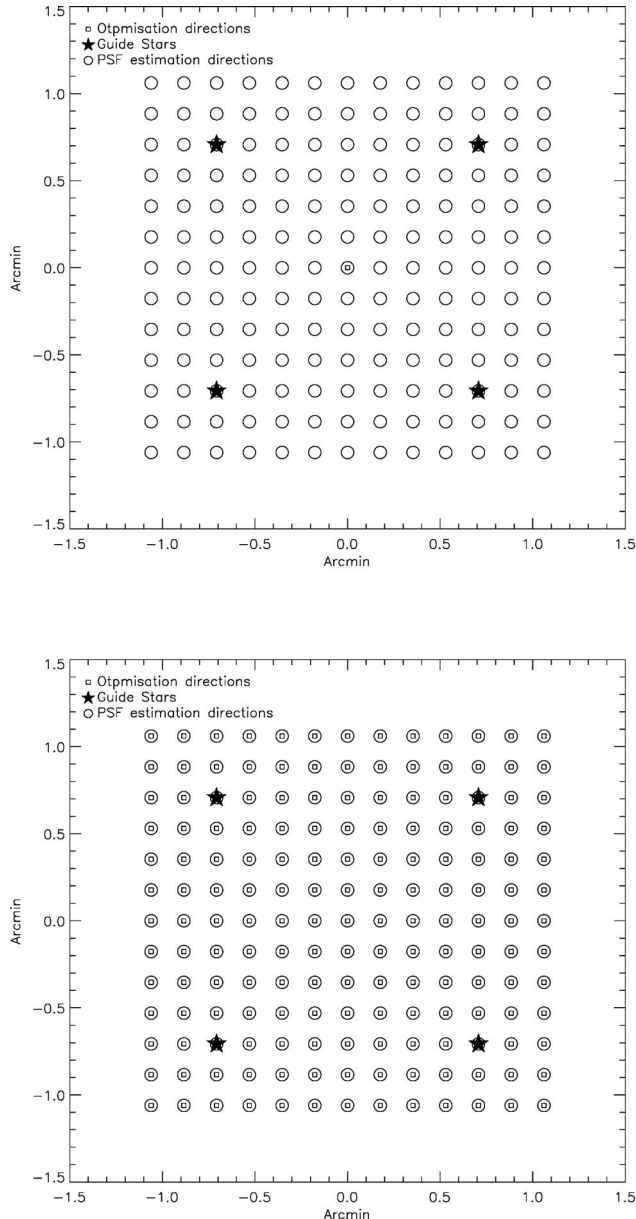
Fig. 16.   Geometry used in the simulations. Top, one direction of optimization is considered at the center of the field. Bottom, optimization is performed over the entire field.

lence volume. The correction is then applied with one DM conjugated to the pupil per science channel: $\mathbf{P}_\theta^{DM} = \mathbf{Id}$. For LTAO, only one science channel is considered; for MOAO, few channels are corrected at the same time. For each direction of optimization β, the projection onto the DM is simply written as

$$\mathbf{P_{opt}} = \mathbf{P}_\beta^L. \qquad (28)$$

In those directions, the performance is that of the pure tomographic reconstruction described in Section 5; there is no supplementary term of error due to generalized fitting. An example of the expected performance of an LTAO/MOAO system is presented in Fig. 17 (top) for the 4GS case. In this example, only one direction at the center of the field ($\beta = 0$) has been optimized. For this direction, the performance is limited only by unseen frequencies and
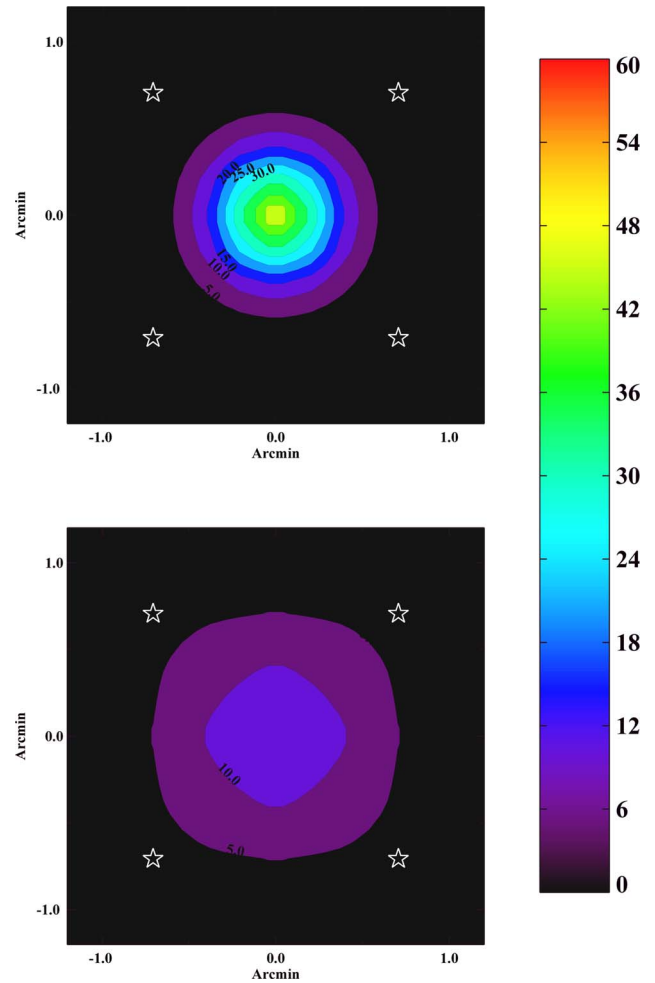

Fig. 17.   (Color online) SR maps for MOAO (top) and GLAO (bottom). GS are 45° rotated compared with Table 2. The SR have been linearly interpolated on a 26×26 grid. For MOAO, the SR is $\sim 50\%$ at the center of the field. For GLAO, the SR is $\sim 10\%$ at the center of the field.

reaches $\sim 50\%$ of SR. Outside this direction, performance decreases quickly due to classical anisoplanatism.

B. GLAO
With still one DM conjugated to the telescope pupil but an optimization in the whole field, we now investigate GLAO [28]. The GLAO correction represents the worst case for generalized fitting, as only one DM is used to correct the whole FoV. For a DM conjugated to the telescope pupil, $\mathbf{P}_{\beta_j}^{DM}$ simply becomes the identity matrix, and the projection term then is written as

$$\mathbf{P_{opt}} = \langle \mathbf{P}_{\beta_j}^L \rangle_\beta, \qquad (29)$$

which represents only an average over the entire direction of optimization. An example of the expected performance with GLAO is presented in Fig. 17 (bottom). We see that the performance is limited to few percent of SR, but it is almost uniform in the field, and the corrected area is larger than for the MOAO correction. For this example, the error due to generalized fitting at the center of the FoV can be as high as a factor of 5.

C. MCAO
To reduce the projection error, one must use more DMs optically conjugated to the layers in altitude.

1. Generalized Fitting
When several DMs are used to perform the correction, the projection term is given by Eq. (21). For a given optimized field, the generalized fitting error depends only on the number of DMs [12,13]. The more DMs used to correct the volume and the better the match between the mirrors' positions and the turbulent layers, the better the performance in the field.

To illustrate the effect of the generalized fitting error, in Fig. 18 we plot the mean SR over the field (computed over the 169 directions) as a function of the number of DMs. Error bars represent the standard deviation of the SR in the field. The altitudes of the DMs are defined by the altitudes of the equivalent layers, following the same procedure as in Subsection 6.B. Results are shown for the 4GS and 8GS cases using an MMSE reconstruction.

Figure 18 shows that with the 4GS (medium-FoV) case, 3 DMs are sufficient to obtain an almost optimal performance. However, for the 8GS (large-FoV) case, this number increase to 8 DMs. These results are very similar to those obtained in Fig. 6(b). Indeed, as introduced by Fusco *et al.* [4], the generalized fitting error is close to the model error on the number of layers.

2. Effect of Different Reconstructors
We now want to investigate the gain of the regularized reconstructor (MMSE) compared with the TLSE one. We use the 4GS case with 3 DMs located, respectively, at [0,3.5,9.3] km to limit the effect of generalized fitting (see Fig. 18). In Fig. 19 we show the SR map for the TLSE (top) and MMSE (bottom) approach. We find that the MMSE provides a performance ~1.2 times better in mean SR: there is a significant gain in using a regularized algorithm compared with using a crude TLSE one. This is true particularly in the corners of the field where the MMSE extrapolates the phase estimation, whereas the TLSE becomes very sensitive to unseen frequencies. Note that in the TLSE case, another choice of threshold could
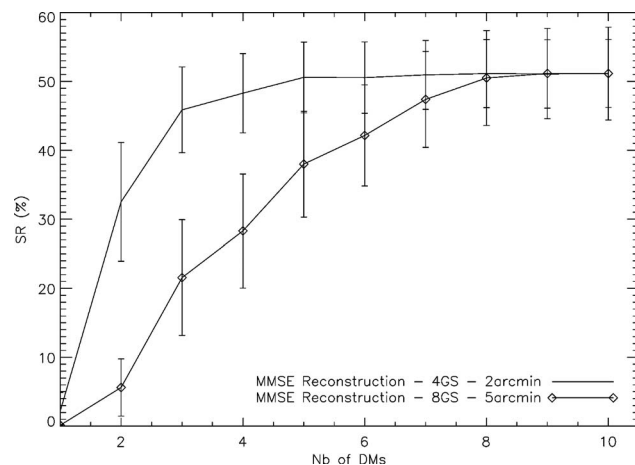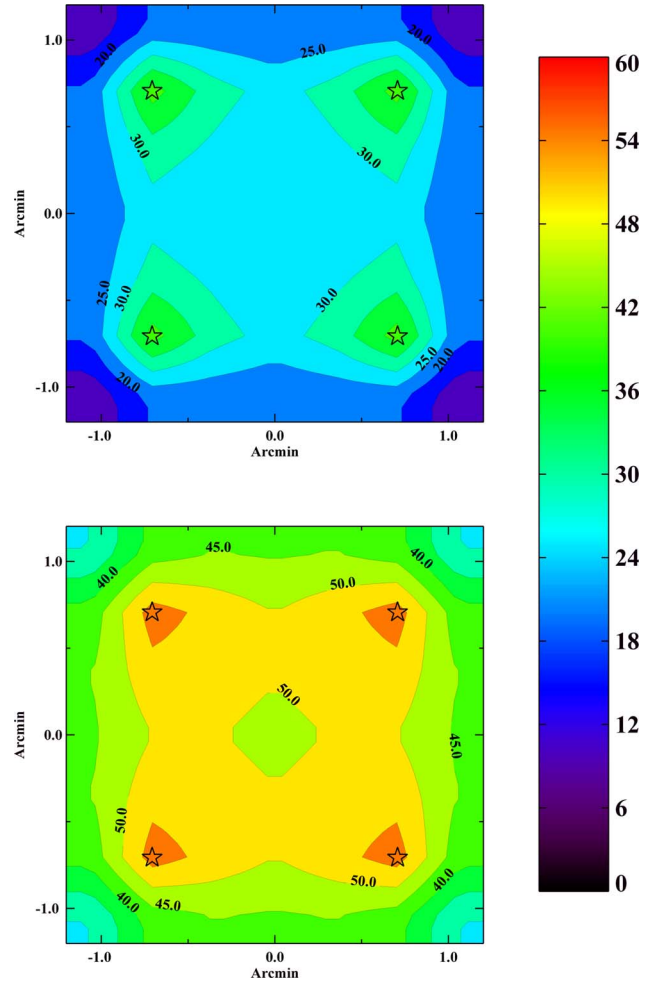

Fig. 19.   (Color online) SR maps for an MCAO working with 3 DMs at [0,3.5,9.3] km. Comparison between TLSE (top) and MMSE (bottom) reconstructors. SR[min,max,mean,standard deviation] =[10%,42%,25%,6%] for the TLSE and [30%, 57%, 47%, 6%] for MMSE.

make the performance better on the GS (as good as with the MMSE reconstruction), at the cost of decreasing the performance in the field.

3. Equivalent Layers
Another classical approach in MCAO is to reconstruct the turbulence volume only at the DMs' altitudes. No projection onto the DMs is then required, and $\mathbf{P_{opt}}=\mathbf{Id}$. Following our approach, this is none other than the model error on the number of layers as described in Subsection 6.B. Whereas in Subsection 6.B we focused on the effect of this error at the center of the field, we now want to evaluate the effect of this approach on the performance in the whole field. We choose to simulate a system working with 3 DMs as described in Subsection 8.C.2. In Fig. 20 we compare the performance obtained for the TLSE (top) and for the MMSE (bottom) reconstructors.

Similarly to the results of Subsection 8.C.2, we first find that the MMSE approach provides a performance ~1.2 times better than the TLSE one. Another interesting exercise is to compare the results of Fig. 20 with those of Fig. 19. Doing so, we first find that the mean SRs are very close for the two approaches: a reconstruction performed

Fig. 18.   Mean SR over the field in function of the number of DMs. Error bars represent the standard deviation of the SR.
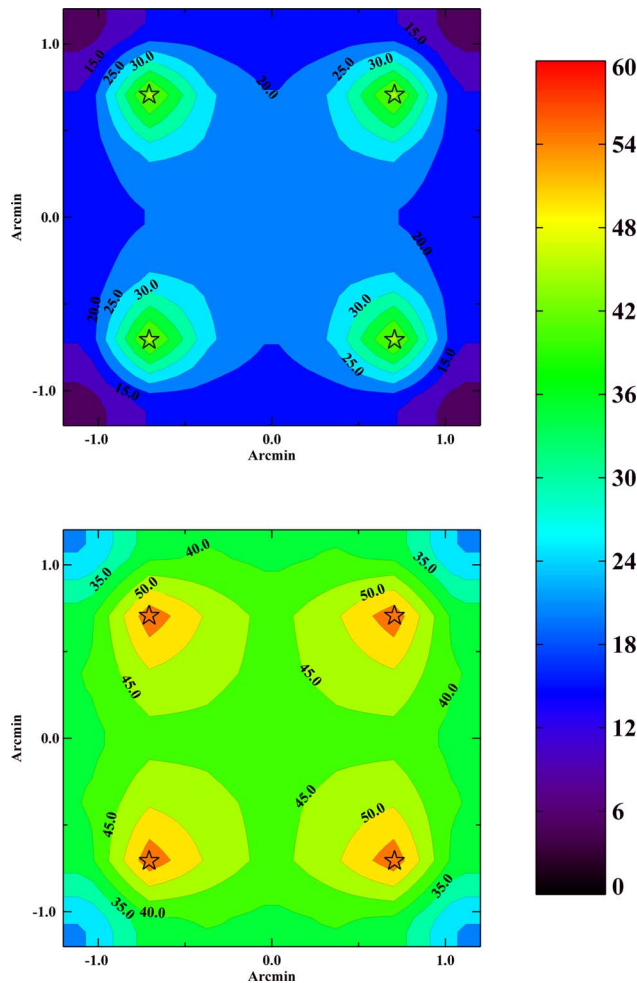
Fig. 20. (Color online) SR MMSE in the EL approach: turbulence volume is reconstructed only at DMs' altitudes. Top, TLSE reconstructor SR[min,max,mean,standard deviation]=[7%,47%,21%,7%]. Bottom, MMSE reconstructor. SR[min,max,mean,standard deviation]=[24%,58%,42%,6%].

directly on the DMs gives only a 5% lower performance in SR. This is indeed consistent with the results obtained in Fig. 11 for the center of the field. Note that this error depends strongly on the turbulence profile, and different turbulence conditions would give different results. In any case, the main difference between Fig. 20 and Fig. 19 is that the correction is no longer uniform over the field when one uses a reconstruction directly onto the DMs. Indeed, the optimization of the performance for specific directions comes from the projection term $\mathbf{P_{opt}}$. To enable an optimization of the performance in the field, one must then reconstruct the turbulence volume on more layers than DMs. The other main drawback of a reconstruction directly on the DMs is that the corresponding model error is very sensitive for large-FoV systems (see Subsection 6.B). For instance, the same study for the 8GS configuration gives a mean SR of only 15% for the MMSE reconstructor. The main advantage of the EL approach is that the tomography is much more simplified than with the full MCAO presented in Subsection 8.C.2.

9. CONCLUSION

We have presented a matrix formalism for the Fourier modeling of any WFAO system. Our Fourier tool includes all the specifies of the WFAO systems such as tomography, number/positions of DMs, and model/statistical errors. The Fourier approach is interesting because it allows a fast and easy exploration of the broad parameter space as well as a detailed comprehension of the underlying physical phenomena. For ELT studies, it offers a fine and accurate modeling tool, able to provide the end product PSFs.

With this Fourier tool, we have explored three main issues of any WFAO system: unseen frequencies, model/ statistical errors, and projection errors. Our goal was not to derive numerical results but rather to point out general trends shared by the tomographic systems. We first illustrated how the GS geometry set the amount of unseen frequencies. The distribution of unseen frequencies is essential to understanding the additional errors: they represent the roots of additional errors. Our exploration of model/statistical errors reveals several limitations shared by all WFAO systems. First, we find that the MMSE approach is always more accurate and robust than the best TLSE one. Second, we find that the tomographic reconstruction is robust to statistical errors but is very sensitive to model errors. For medium-FoV systems, a good knowledge of statistical/atmospheric priors is not essential. However, for large-FoV systems the sensitivity to turbulence distribution errors becomes significant. This implies that large-FoV concepts would require a large number of GSs to limit unseen frequencies or a good monitoring of turbulence conditions.

We also derive few rules for a robust control when system and atmospheric conditions are not perfectly known. In such cases, it is advised to (i) overestimate noise variance, (ii) undererestimate turbulence strength, (iii) tend to a constant turbulence profile strength, and (iv) use more layers in the reconstruction. Finally, we give an initial insight into typical performance of future WFAO systems for ELTs, and we show that regularized tomographic algorithms are essential to provide a significant gain in performance for these future systems.

REFERENCES

1. M. Tallon and R. Foy, "Adaptive telescope with laser probe—Isoplanatism and cone effect," Astron. Astrophys. **235**, 549–557 (1990).
2. D. C. Johnston and B. M. Welsh, "Analysis of multiconjugate adaptive optics," J. Opt. Soc. Am. A **11**, 394–408 (1994).
3. B. L. Ellerbroek, "First-order performance evaluation of adaptive-optics systems for atmospheric-turbulence

compensation in extended-field-of-view astronomical telescopes," J. Opt. Soc. Am. A **11**, 783–805 (1994).

4. T. Fusco, J.-M. Conan, G. Rousset, L. M. Mugnier, and V. Michau, "Optimal wave-front reconstruction strategies for multiconjugate adaptive optics," J. Opt. Soc. Am. A **18**, 2527–2538 (2001).

5. A. Tokovinin, M. Le Louarn, E. Viard, N. Hubin, and R. Conan, "Optimized modal tomography in adaptive optics," Astron. Astrophys. **378**, 710–721 (2001).

6. T. Fusco, J.-M. Conan, V. Michau, G. Rousset, and L. Mugnier, "Isoplanatic angle and optimal guide star separation for multiconjugate adaptive optics," Proc. SPIE **4007**, 1044–1055 (2000).

7. B. Neichel, T. Fusco, J.-M. Conan, C. Petit, and G. Rousset, "PSD based simulation algorithm for Wide FoV AO design. Application to ELT studies," Proc. SPIE **7015**, 701573 (2008).

8. J.-M. Conan, B. Le Roux, D. Bello, T. Fusco, and G. Rousset, "Optimal reconstruction in multiconjugate adaptive optics," in *Beyond Conventional Adaptive Optics: ESO Conference and Workshop* (European Southern Observatory, 2002), Vol. 58, pp. 209–215.

9. A. Tokovinin and E. Viard, "Limiting precision of tomographic phase estimation," J. Opt. Soc. Am. A **18**, 873–882 (2001).

10. M. Le Louarn and M. Tallon, "Analysis of modes and behavior of a multiconjugate adaptive optics system," J. Opt. Soc. Am. A **19**, 912–925 (2002).

11. T. Fusco, J.-M. Conan, V. Michau, L. Mugnier, and G. Rousset, "Efficient phase estimation for large-field-of-view adaptive optics," Opt. Lett. **24**, 1472–1474 (1999).

12. F. Rigaut, B. Ellerbroek, and R. Flicker, "Principles, limitations, and performance of multiconjugate adaptive optics," Proc. SPIE **4007**, 1022–1031 (2000).

13. A. Tokovinin, M. Le Louarn, and M. Sarazin, "Isoplanatism in a multiconjugate adaptive optics system," J. Opt. Soc. Am. A **17**, 1819–1827 (2000).

14. F. Rigaut, J.-P. Veran, and O. Lai, "Analytical model for Shack–Hartmann-based adaptive optics systems," Proc. SPIE **3353**, 1038–1048 (1998).

15. L. Jolissaint, J.-P. Veran, and R. Conan, "Analytical modeling of adaptive optics: foundations of the phase spatial power spectrum approach," J. Opt. Soc. Am. A **23**, 382–394 (2006).

16. T. Fusco, J.-M. Conan, V. Michau, and G. Rousset, "Noise propagation for multiconjugate adaptive optics system," Proc. SPIE **4538**, 144–155 (2002).

17. D. T. Gavel, "Tomography for multiconjugate adaptive optics systems using laser guide stars," Proc. SPIE **5490**, 1356–1373 (2004).

18. B. L. Ellerbroek, "Adaptive optics without borders: performance evaluation in the infinite aperture limit," Proc. SPIE **5490**, 625–636 (2004).

19. B. L. Ellerbroek, "Linear systems modeling of adaptive optics in the spatial-frequency domain," J. Opt. Soc. Am. A **22**, 310–322 (2005).

20. C. Vérinaud, "On the nature of the measurements provided by a pyramid wave-front sensor," Opt. Commun. **233**, 27–38 (2004).

21. A. Tarantola and B. Valette, "Generalized nonlinear inverse problems solved using the least squares criterion," Rev. Geophys. Space Phys. **20**, 219–232 (1982).

22. F. Rigaut and E. Gendron, "Laser guide star in adaptive optics: the tilt determination problem," Astron. Astrophys. **261**, 677–684 (1992).

23. R. Ragazzoni, "Multiple field of view layer oriented," in *Beyond Conventional Adaptive Optics: ESO Conference and Workshop* (European Southern Observatory, 2001), Vol. 58, pp. 75–82.

24. C. Petit, J.-M. Conan, C. Kulcsár, and H.-F. Raynaud, ONERA, BP72, Chatillon FR-92322, are preparing a manuscript to be called, "LQG control for AO and MCAO: experimental and numerical analysis."

25. A. Tokovinin, "Performance and error budget of a GLAO system," Proc. SPIE **7015**, 701526 (2008).

26. F. Hammer, F. Sayede, E. Gendron, T. Fusco, D. Burgarella, V. Cayatte, J.-M. Conan, F. Courbin, H. Flores, I. Guinouard, L. Jocou, A. Lançon, G. Monnet, M. Mouchine, F. Rigaud, D. Rouan, G. Rousset, V. Buat, and F. Zamkotsian, "The FALCON concept: multi-object spectroscopy combined with MCAO in near-IR," in *Beyond Conventional Adaptive Optics: ESO Conference and Workshop* (European Southern Observatory, 2002), Vol. 58, pp. 139–148.

27. F. Assémat, E. Gendron, and F. Hammer, "The FALCON concept: multi-object adaptive optics and atmospheric tomography for integral field spectroscopy—principles and performance on an 8-m telescope," Mon. Not. R. Astron. Soc. **376**, 287–312 (2007).

28. F. Rigaut, "Ground conjugate wide field adaptive optics for the ELTs," in *Beyond Conventional Adaptive Optics: ESO Conference and Workshop* (European Southern Observatory, 2002), Vol. 58, pp. 11–16.